Weak Lensing Measurement of the Mass–Richness Relation of SDSS redMaPPer Clusters

Melanie Simet[1]*, Tom McClintock[2], Rachel Mandelbaum[1], Eduardo Rozo[2], Eli Rykoff[3], Erin Sheldon[4], Risa H. Wechsler [3,5]

[1] *McWilliams Center for Cosmology, Carnegie Mellon University, 5000 Forbes Ave, Pittsburgh PA 15213, USA*
[2] *Department of Physics, University of Arizona, 1118 E. Fourth St., Tucson, AZ 85721, USA*
[3] *Kavli Institute for Particle Astrophysics and Cosmology, SLAC National Accelerator Laboratory, Menlo Park, CA 94305, USA*
[4] *Brookhaven National Laboratory, Bldg 510, Upton, NY 11973, USA*
[5] *Department of Physics, Stanford University, 452 Lomita Mall, Stanford, CA 94305-4085, USA*

5 April 2017

ABSTRACT

We perform a measurement of the mass–richness relation of the redMaPPer galaxy cluster catalogue using weak lensing data from the Sloan Digital Sky Survey. We have carefully characterized a broad range of systematic uncertainties, including shear calibration errors, photo-z biases, dilution by member galaxies, source obscuration, magnification bias, incorrect assumptions about cluster mass profiles, cluster centering, halo triaxiality, and projection effects. We also compare measurements of the lensing signal from two independently-produced shear and photometric redshift catalogues to characterize systematic errors in the lensing signal itself. Using a sample of 5,570 clusters from $0.1 \leqslant z \leqslant 0.33$, the normalization of our power-law mass vs. λ relation is $\log_{10}[M_{200m}/h^{-1}\ M_\odot] = 14.344 \pm 0.021$ (statistical) ± 0.023 (systematic) at a richness $\lambda = 40$, a 7 per cent calibration uncertainty, with a power-law index of $1.33^{+0.09}_{-0.10}$ (1σ). The detailed systematics characterization in this work renders it the definitive weak lensing mass calibration for SDSS redMaPPer clusters at this time.

Key words: gravitational lensing: weak, galaxies: clusters: general

1 INTRODUCTION

The abundance of galaxy clusters is a powerful cosmological probe (Albrecht et al. 2006). In this work, we measure the relationship between the weak lensing masses and the optical richness of galaxy clusters. Weak lensing offers a unique key to understanding the masses of structures in the universe, due to its equal sensitivity to dark and baryonic matter (Schneider 2006). Galaxy clusters are a good target for weak lensing due to their high masses and thus large lensing distortions. Using weak lensing mass measurements, then, we can better understand the relationship between cluster masses and other observables, which aids scientific goals such as measurements of cluster abundances for cosmology.

Weak lensing exploits the deflection of light rays and the resulting distortion of galaxy shapes by gravitational fields. By measuring statistical changes in the shapes of more distant galaxies, we can detect the gravitational fields sourced by intervening matter and therefore probe the distribution and amount of matter in the universe (Schneider 2006). Weak lensing has been commonly used to characterize the matter in galaxies (e.g. Brainerd et al. 1996), groups (e.g. Leauthaud et al. 2010) and galaxy clusters (e.g. Sheldon et al. 2004a; Johnston et al. 2007a; von der Linden et al. 2014; Hoekstra et al. 2015; Okabe & Smith 2015; van Uitert et al. 2016), as well as the large-scale distribution of matter through the technique known as cosmic shear (e.g. Bacon et al. 2000; Kilbinger et al. 2013; Becker et al. 2016).

Galaxy clusters, the target of this weak lensing study, represent the most massive gravitationally bound structures in the universe (e.g., Allen et al. 2011). They consist of multiple galaxies in a large dark matter halo, usually with one large elliptical galaxy in the centre. These galaxies are systematically different from other elliptical galaxies (e.g. von der Linden et al. 2007). The dominant baryonic component is a reservoir of hot gas held by the potential well of the dark matter halo, but this gas is visible only in the X-ray (thermal Bremsstrahlung) and radio (through scattering of photons from the cosmic microwave background). All of these properties can be used to construct cluster catalogues, based on characteristics such as distortions of the observed spectrum

*Now at: Department of Physics and Astronomy, University of California, Riverside, CA 92507

of CMB photons along the line of sight to the clusters (Bleem et al. 2015), extended X-ray emission (Piccinotti et al. 1982), or simply an overdensity of optically-detected galaxies at the same redshift. In this paper, we use the redMaPPer optical cluster finder (Rykoff et al. 2014, henceforth RM I), described in Sec. 3.1. Cluster catalogues typically have a ranking mechanism based on a mass proxy such as X-ray luminosity or the number of galaxies in the cluster. We calibrate the relationship between the redMaPPer mass proxy, the summed galaxy membership probability λ (also known as the optical richness), and the masses derived from weak lensing measurements.

Previous work on the redMaPPer catalogue mass–richness relation has included comparison to other cluster data sets and weak lensing measurements from several different imaging surveys (Rozo & Rykoff 2014; Saro et al. 2015; Miyatake et al. 2016; Du et al. 2015). Due to widely varying parameterization choices, we will discuss these results further in Section 7, including conversions necessary to compare amongst them and against our work. The work presented here is the largest sample for which such measurements have been made; we obtain high signal-to-noise measurements of the lensing signal in several richness bins and two redshift bins, and also use what we believe to be the most complete model for the lensing signal and its systematics. Our results are consistent with previous measurements, but precisely calibrate the systematic uncertainty associated with the weak lensing masses.

We discuss the background of our weak lensing procedure in Sec. 2. We then discuss the redMaPPer algorithm and its application to SDSS DR8 data, particularly its richness estimator λ, in Sec. 3.1. The lensing shear catalogue is described in Sec. 3.2. The mass model that we use is detailed in Sec. 4, and we address a variety of sources of systematic error in Sec. 5. Our results from model fits are given in Sec. 6. We summarize and conclude in Sec. 7. Throughout the paper, except where noted, we assume a flat ΛCDM cosmological model with $\Omega_m = 0.3$, $\sigma_8 = 0.8$, and $h_{100} = 1$. Unless otherwise specified, all distances are physical distances (rather than comoving).

2 WEAK LENSING BACKGROUND

The deflection of light by gravity affects the apparent shape, size, and number density of galaxies. These effects can be used to measure the relationship between dark matter and visible matter, or more generally to probe cosmological models (Bartelmann & Schneider 2001; Huterer 2002; Hu 2002; Abazajian & Dodelson 2003; Refregier 2003; Schneider 2006; Hoekstra & Jain 2008; Massey et al. 2010). An overdensity of matter, such as a galaxy or galaxy cluster, will cause a slight tangential alignment of galaxies at more distant redshifts; an underdensity, such as a void, will cause a slight radial alignment. In addition, the number density (e.g. Broadhurst et al. 1995) or distribution of quantities such as redshift (e.g. Coupon et al. 2013) and size (e.g. Schmidt et al. 2009) will be altered, due to effects that shrink or enlarge the galaxy images on the sky. Shape distortion is usually called the lensing shear, while the other effects come under the umbrella of lensing magnification. Since weak lensing (as opposed to strong lensing) results in only slight differences in observed galaxy properties, it must be measured statistically.

For galaxy cluster lensing, we are well within the thin-lens limit, where the line-of-sight extent of the lens is much smaller than distances between the observer and the lens, and between the lens and the lensed galaxy. When considering lensing shear, we are sensitive to the surface mass density $\Sigma(R)$, where R here is the projected separation on the sky from the lens, calculated as the angular diameter distance $D_A(z)$ times the angular separation between the centre of the lens and the lensed galaxy. The tangential shear $\gamma_t(R)$ imposed by a lens at redshift z_l on a background source at redshift z is given by (Schneider 2006)

$$\gamma_t(R) = \frac{\bar{\Sigma}(< R) - \bar{\Sigma}(R)}{\Sigma_{\rm cr}(z_l, z)}, \tag{1}$$

that is, the average surface mass density interior to the radius R minus the average surface mass density in an annulus at radius R, modulated by a geometric factor known as the critical surface mass density:

$$\Sigma_{\rm cr}(z_l, z) = \frac{c^2}{4\pi G} \frac{D_A(z)}{D_A(z_l) D_A(z_l, z)}. \tag{2}$$

In practice, since we use lenses and sources at many different redshifts, we formulate the problem as an estimate of $\Delta\Sigma$ (McKay et al. 2001),

$$\Delta\Sigma \equiv \Sigma_{\rm cr}(z_l, z)\gamma_t(R) = \bar{\Sigma}(< R) - \bar{\Sigma}(R), \tag{3}$$

which, being directly related to the projected mass profile around the lens, is the same for identical lenses regardless of the lens and source redshifts.

Since the lensing-induced shear is significantly smaller than the intrinsic scatter in galaxy shapes, we use a statistical estimator that sums over all background (lensed) galaxies i found within an annulus centred at radius R around the lens:

$$\widehat{\Delta\Sigma}(R) = C(R)\frac{\sum_i w_i \Sigma_{\rm cr}(z_l, z_i)\gamma_{t,i}}{\sum_i w_i}. \tag{4}$$

The optimal weights w_i above include both the per-object shape noise weighting $w_{i,\rm shape}$ and the critical surface mass density (Sheldon et al. 2004b),

$$w_i = \Sigma_{\rm cr}^{-2} w_{i,\rm shape}, \tag{5}$$

where $w_{i,\rm shape} = 1/(\sigma_{\rm int}^2 + \sigma_i^2)$ includes both intrinsic shape noise and measurement uncertainty. The per-object shape noise is a product of our shape measurement and is described in Section 3.2. The inclusion of the critical surface mass density optimally accounts for the different lensing geometries of galaxies at different redshifts, though the effects of photometric redshift error prevent us from achieving an optimal measurement (Mandelbaum et al. 2008b). We explicitly cancel out factors of $\Sigma_{\rm cr}$ in the numerator of Equation (4) to highlight that the summand converges to 0 as z_i approaches z_l from above.

In practice, we compute the average signal for many lenses at once. This increases our signal-to-noise ratio and also reduces biases due to individual characteristics of the lens (such as extra line-of-sight overdensities, lens substructure, and lens asphericity) by averaging those properties as well (e.g. Johnston et al. 2007b; Corless & King 2009). So,

for a bin containing lenses j, we in fact have

$$\widehat{\Delta\Sigma}(R) = C(R)\frac{\sum_{i,j} w_{ij}\Sigma_{\mathrm{cr},ij}\gamma_{t,i}}{\sum_{i,j} w_{ij}}. \qquad (6)$$

We include a boost factor $C(R)$ to account for contamination of our background galaxy sample by galaxies that are physically associated with the cluster (Fischer et al. 2000). Our background galaxy source sample is photometric, with the catalogue described in Section 3.2. Because of the scatter in the photometric redshift estimates, some galaxies located in the cluster will be scattered into the background sample; these galaxies have a shear expectation value of 0, unlike the lensed background galaxies, so they will dilute the measured lensing signal. This is a particular problem for galaxy clusters, since they contain many galaxies that can be scattered this way. To correct for the dilution effect from cluster galaxies in the source population, we compute the weighted number density of sources around random points (described in Section 3.1) using the weights from Eq. (5). For background galaxies i around N lenses j, and background galaxies k around N_{rand} random points l:

$$C(R) = \frac{N_{\mathrm{rand}}}{N}\frac{\sum_{i,j} w_{ij}}{\sum_{k,l} w_{kl}}. \qquad (7)$$

This multiplicative correction is performed on a per-bin basis, and ranges from 1.2-1.4 in the innermost radial bin used for fitting in the lower-redshift cluster bins or from 1.4-1.7 in the innermost radial bin used for fitting in the higher-redshift cluster bins. We note that the above correction factor can be explicitly demonstrated to be correct (Rozo et al. 2011), and is commonly used in statistical lensing measurements (e.g., Sheldon et al. 2004b; Mandelbaum et al. 2005, and associated follow-up work). Indeed, this is one of the great advantages of using photometric survey data and treating weak lensing as a statistical measurement; by using a stack of many objects for which the source density converges to a well-understood average across the survey, we can measure and correct for this contamination very accurately without worrying about statistical fluctuations in the populations behind individual clusters, and without having to use overly-conservative cuts that may risk removing many lensed objects.

To account for the survey mask, which otherwise might impose a small signal at large radii due to systematic errors that correlate with the survey boundaries, we subtract the $\Delta\Sigma$ estimate around random points from our real signal before the boost factor is applied (see, e.g., Mandelbaum et al. 2005, 2013), also on a per-bin basis.

3 DATA

In this work, we use data from the Sloan Digital Sky Survey (SDSS; Eisenstein et al. 2011; York et al. 2000). Both our cluster and weak lensing catalogues derive from data release 8 (SDSS DR8 Aihara et al. 2011).

3.1 The redMaPPer Cluster Catalogue

redMaPPer is a red-sequence photometric cluster finding algorithm (Rykoff et al. 2014, hereafter RM I), built around the optimized richness estimator developed in Rozo et al.

(2009b) and Rykoff et al. (2012). Briefly, redMaPPer identifies galaxy clusters as overdensities of red galaxies, and estimates the probability that each red galaxy is a cluster member following a matched filter approach which models the galaxy distribution as the sum of a cluster and background component. The cluster richness λ is the sum-total of the membership probabilities of all the galaxies. The cluster radius R_λ used for estimating the cluster richness is self-consistently computed with the cluster richness, ensuring that richer clusters have larger cluster radii. The radius R_λ is selected to maximize the signal-to-noise of the richness measurements. The redMaPPer cluster richness λ has been shown to be tightly correlated with cluster mass by comparing λ to well-known mass proxies such as X-ray gas mass and SZ decrements. The original (v5.2) redMaPPer algorithm was published in RM I, to which the reader is referred for further details. Here, we utilize the v5.10 version of the algorithm, which introduced a variety of small improvements; we refer the reader to Rozo et al. (2015b, hereafter RM IV) for details.

The redMaPPer algorithm was applied to SDSS DR8 data (Aihara et al. 2011) in RM IV. The redMaPPer catalogue is restricted to the $\sim 10,000$ deg^2 of contiguous imaging used by the Baryon Oscillation Spectroscopic Survey (BOSS; Dawson et al. 2013). Roughly 2/3 of the survey falls in the Northern Galactic cap, and 1/3 in the South. The sky was imaged in 5 bands ($ugriz$), and we have imposed a limiting magnitude $i < 21$, which is a conservative estimate for the full footprint (see Rykoff et al. 2015). redMaPPer utilizes the 5-band imaging data to self-calibrate a model for red-sequence galaxies, and then applies this model to identify red galaxy overdensities and to estimate the corresponding photometric redshift of the galaxy clusters. SDSS redMaPPer photometric redshifts are accurate at the 0.005 to 0.01 level, depending on redshift. Here, we ignore the uncertainty associated with the cluster photometric errors. We have verified that randomly perturbing every cluster by its assigned photometric redshift uncertainty impacts our conclusions at less than the 1% level, demonstrating that the cluster photo-z uncertainties are indeed negligible for this analysis.

The redMaPPer algorithm explicitly assumes that the centre of each cluster's halo coincides with the location of one of the brightest galaxies in the cluster, though not necessarily the brightest. Indeed, an important feature of redMaPPer is that it does not simply choose a cluster centre, it also attempts to estimate the probability p_{cen} that each redMaPPer cluster is properly centred. The probability is estimated based on each galaxy's luminosity, photometric redshift, and local galaxy density. redMaPPer relies on a Bayesian classification scheme with empirical, self-calibrated filters for the distribution of central and satellite galaxy properties, modified to take into account that every cluster contains one and only one central galaxy. For details, we refer the reader to RM I. Given the probability p_{cen} for each cluster, the fraction of well-centred clusters over the entire cluster catalogue is simply $P_{\mathrm{cen}} = N_{\mathrm{clusters}}^{-1}\sum p_{\mathrm{cen}}$, where the sum is over all clusters in the catalogue. As discussed in section 5.2, the fraction P_{cen} is an important systematic parameter in our analysis.

Cluster random points were generated using the updated method of Rykoff et al. (2016). In brief, we first sample

a cluster from the redMaPPer cluster catalogue. This gives us the richness and redshift of our random point. We then randomly select a right ascension and declination within the survey footprint. If the survey is not sufficiently deep to have detected a cluster at that location, we reject the cluster, while keeping track of the number of times N_R which each cluster is rejected. If the survey is sufficiently deep to detect our randomly selected cluster, then the cluster is added to the random catalogue at the randomly drawn position. The procedure is iterated until the random catalogue achieves the desired number of random points. Let N be the number of times that a particular cluster appears in the random catalogue, and N' by the number of times the cluster was rejected as a random point. We assign a weight $w = (N + N')/N$ to each instance of this cluster in the random catalogue. This ensures that the weighted random catalogue exactly traces the richness and redshift distribution of the parent cluster catalogue.

To perform the weak lensing measurement, we bin the clusters in 4 richness bins and 2 redshift bins, for a total of 8 bins. The bins are detailed in Table 1. We note that the largest bin has a very broad range of λ, but we checked alternate binning schemes and found no statistically significant differences between our final results. Our fiducial binning scheme has roughly equal signal-to-noise for all richness and redshift bins.

3.2 Lensing data

We use a shear catalogue first presented in Reyes et al. (2012), covering approximately 9,000 square degrees and containing 39 million galaxies, or 1.2 galaxies/arcmin^2. This catalogue derives from Sloan Digital Sky Survey images as of Data Release 8 (York et al. 2000; Aihara et al. 2011). The images were analyzed with the re-Gaussianization algorithm[1] (Hirata & Seljak 2003), which calculates adaptive second-order moments for the galaxy and point-spread function (PSF) by fitting elliptical Gaussians to the images, and then combines these moments and a correction for low-order non-Gaussianity to produce a measured distortion e. We are interested in lensing shears, not distortions[2], so we must correct for the difference, and also for the fact that shears do not add linearly (Bernstein & Jarvis 2002). The average sensitivity of the mean distortion of the shape sample to an applied shear is usually called the responsivity, which for unweighted measurements is $\mathcal{R} \approx 1 - e_{\mathrm{rms}}^2$. For this catalogue the appropriate value of e_{rms} is 0.365 (Reyes et al. 2012). We use the approximation here and not a full calculation of $\mathcal{R}$, but our value is consistent with the more detailed analysis. We also apply a multiplicative shear calibration factor of 1.02, as discussed in Mandelbaum et al. (2013). Further characterization of the systematic errors in this catalogue was carried out in Mandelbaum et al. (2012) and Mandelbaum et al. (2013).

---

[1] An updated version of the software that was used to produce this catalogue is publicly available as part of the `GalSim` package (Rowe et al. 2015): https://github.com/GalSim-developers/GalSim.
[2] The difference is merely a parameterization choice — a shear is a ratio of linear functions of the axis ratio of the ellipse, while a distortion is a ratio of functions of the axis ratio squared.

The photometric redshifts in this catalogue were calculated using the Zurich Extragalactic Bayesian Redshift Analyzer, or ZEBRA (Feldmann et al. 2006). ZEBRA is a template-fitting software; for this catalogue, four observed SEDs and two synthetic blue galaxy spectra from Benítez (2000) were used, along with twenty-five additional interpolated templates created between pairs of the six original templates. The performance of the photometric redshifts and their impact on weak lensing measurements was explored by Nakajima et al. (2012). The starburst-type galaxies, accounting for approximately 10 per cent of the original sample, were found to be unreliable based on comparison with a reference sample and were removed from the final catalogue. There is a remaining known bias for galaxies with $z \gtrsim 0.4$. We know the true $\mathrm{d}N/\mathrm{d}z$ based on the work of Nakajima et al. 2012, so we can correct the effect of bias and scatter if we know the lens redshifts in the sample. This bias is worse as redshift increases; it is 3 per cent for the distribution of cluster redshifts in our lower redshift bin ($z = 0.1 - 0.2$) and 11 per cent for the distribution of cluster redshifts in our higher redshift bin ($z = 0.2 - 0.33$). All results shown in this paper have these corrections applied. The associated systematic uncertainty on $\Delta\Sigma$ is 2 per cent. The uncertainty in the amplitude of the $\Delta\Sigma$ profile due to the use of photometric redshifts was estimated by comparing the different lensing amplitudes for the source population as estimated using representative spectroscopy from a variety of different spectroscopic surveys. The differences in the source redshift distribution between the different spectroscopic surveys reflects cosmic variance, and is the main limitation of our method. For further details, we refer the reader to Nakajima et al. (2012).

4   MASS MODELING

In this section, we discuss the cluster mass model we will use to analyze the data. We exclude small scale data to minimize systematic uncertainties, particularly with regards to membership dilution, strong shear, and galaxy obscuration by member galaxies. The scales we use are also large enough that the stellar mass component associated with the central galaxy is negligible, and can be safely ignored. Consequently, we model the mass contribution from the halo profile only, without adding a component for the central galaxy. We first describe the model for a single cluster dark matter halo (section 4.1) and then address the impact of analyzing multiple halos at once (section 4.2). We summarize the full set of parameters in section 4.3 and describe how we will constrain them using the data.

4.1   The Lensing Profile of Cluster Halos

We assume that the clusters are spherical Navarro-Frenk-White (NFW; Navarro et al. 1997) halos on average. The mass of each cluster is assumed to depend on the cluster richness via a scaling relation, including scatter. The corresponding halo concentrations are computed using a mass–concentration relation, whose amplitude we fit for. In addition, some of the clusters are expected to be improperly centred. We note that while no individual cluster is spherical, the observed lensing signal — i.e. the tangential shear

λ range	mean λ	z range	mean z	mean P_{cen}	No. of clusters
$[20, 30)$	24.1	$[0.1, 0.2)$	0.153	0.87	767
$[20, 30)$	24.1	$[0.2, 0.33)$	0.260	0.87	2531
$[30, 40)$	34.4	$[0.1, 0.2)$	0.154	0.87	306
$[30, 40)$	34.5	$[0.2, 0.33)$	0.259	0.87	940
$[40, 55)$	46.3	$[0.1, 0.2)$	0.156	0.89	178
$[40, 55)$	46.5	$[0.2, 0.33)$	0.259	0.88	449
$[55, 140)$	73.2	$[0.1, 0.2)$	0.152	0.90	104
$[55, 140)$	71.8	$[0.2, 0.33)$	0.257	0.88	295

Table 1. Binning scheme for the redMaPPer clusters and characteristics of the clusters in each bin, including richness λ, redshift z and probability of correct centroid P_{cen}. The typical N_{rand}/N for the random catalogues is ~ 22, and the typical mean richness and redshift are consistent for the randoms to $\lesssim 1$ per cent. All averages are weighted by the same lensing weights we use to generate stacked models.

induced by our galaxy clusters — explicitly depends on the circularly symmetric mass density profile only. That is, we only require that NFWs be an adequate description of the circularly averaged projected mass density profiles.

Spherical NFW clusters have a mass density given by

$$\rho(r) = \frac{\rho_0}{(r/r_s)(1 + r/r_s)^2} \quad (8)$$

([Navarro et al. 1996](#), [1997](#)), where ρ_0 and r_s are two free parameters that fully determine the density profile. We measure cluster mass at a radius r_{200m}, defined such that the mean density interior to this radius is 200 times the mean matter density of the Universe at the redshift of the cluster. That is,

$$\frac{M}{\frac{4\pi}{3} r_{200m}^3} = 200 \bar{\rho}_m(z). \quad (9)$$

One also typically defines the concentration parameter $c = r_{200m}/r_s$. The parameters M and c are uniquely related to ρ_0 and r_s, and are the parameters typically utilized to characterize NFW halos. We will follow that convention in this work.

Our mass definition here is often referred to as M_{200m} to denote the overdensity of 200 and the fact that it is measured relative to the matter density. For simplicity, we refer to M or M_0 in some equations in this work, but this will always be M_{200m}. Where a unit is needed (such as in $\log M_0$), the masses have been measured in $h^{-1}\ M_\odot$ units.

As described in Section [2](#), lensing shear is sensitive to a function of the surface mass density. The surface mass density for NFW halos is analytic ([Bartelmann 1996](#); [Wright & Brainerd 2000](#)), so in the absence of centring errors we could plug this surface mass density directly into Eq. ([3](#)) to fit our model to the data. Centroiding errors introduce a further complication: they convolve the surface mass density with the distribution of centroiding offsets. Given an offset radius of R', the convolution is ([Yang et al. 2006](#); [Johnston et al. 2007b](#))

$$\Sigma(R, M, c, R') = \frac{1}{2\pi} \int_0^{2\pi} d\theta\, \Sigma(\sqrt{R^2 + R'^2 + 2RR'\cos\theta}, M, c) \quad (10)$$

We follow previous authors in adopting a 2D Gaussian miscentring distribution for R' where we denote the Gaussian width as R_{mis} ([Johnston et al. 2007b](#); [van Uitert et al. 2016](#)). The fraction of well-centred clusters is denoted P_{cen}. The

miscentred surface mass density is therefore

$$\Sigma(R, M, c, R_{mis}, P_{cen}) = $$
$$P_{cen}\Sigma(R, M, c)$$
$$+ \frac{1 - P_{cen}}{2\pi} \int_0^\infty dR' \left[\frac{R'}{R_{mis}^2} \exp(-R'^2/2R_{mis}^2) \right.$$
$$\left. \times \int_0^{2\pi} d\theta\, \Sigma(\sqrt{R^2 + R'^2 + 2RR'\cos\theta}, M, c) \right] \quad (11)$$

This expression is plugged into Eq. ([3](#)) to obtain our final model for $\Delta\Sigma$: $\Delta\Sigma(R, M, c, R_{mis}, P_{cen})$. The natural length scale for parametrizing the cluster miscentring offset R_{mis} is the cluster radius R_λ used to search for central galaxies. Consequently, we set $R_{mis} = \tau R_\lambda$, where R_λ is the cluster radius from the redMaPPer algorithm and τ is one of our model parameters. If miscentring traces a satellite galaxy distribution modeled as a singular isothermal sphere, one expects $\tau = \frac{1}{2}$. For NFW halos, we expect $\tau < 1/2$. Our exact priors are detailed in Sec. [5.2](#).

4.2 The Mass–Richness Relation and Stacked Cluster Profiles

In practice, we are not fitting to the lensing profile of individual clusters, but rather a stack of clusters of different redshifts and richnesses. The model we fit to the data is built in a similar way, by stacking the expected lensing signal given the richnesses and redshifts of the clusters that went into the measured lensing signal, along with their miscentring information. The relation between halo mass and cluster richness is given by the probability distribution $P(M|\lambda)$, for which we adopt a log-normal model. We set the mean of this relation via

$$\langle M|\lambda \rangle = M_0 \left(\frac{\lambda}{\lambda_0} \right)^\alpha \quad (12)$$

using a pivot point of $\lambda_0 = 40$. This choice roughly decorrelates our model parameters of scientific interest. In our fiducial model we do not allow for redshift evolution. An extension of our fiducial model that allows for redshift evolution in the scaling relation is presented in Appendix [B](#), where we demonstrate that the data has only minimal constraining power on redshift evolution, and that allowing this additional degree of freedom does not impact the conclusions of this work.

We note that the above parameterization of the

richness–mass relation differs from the more traditional convention of defining the scaling relation parameters via $\langle \ln M|\lambda \rangle = \ln M_0 + \alpha \ln(\lambda/\lambda_0)$. The reason is that unlike the traditional parameterization, Eq. 12 effectively decouples uncertainty in the scatter from uncertainty in the amplitude of the mass–richness relation. If desired, one can go from one choice of parameterization to the other via $\ln\langle M|\lambda \rangle = \langle \ln M|\lambda \rangle + 0.5\mathrm{Var}(M|\lambda)$ (Rozo et al. 2009a).

The variance of the distribution $P(M|\lambda)$ is modeled based on our expectation for the scatter in the converse distribution $P(\lambda|M)$. Specifically, consider a model in which the scatter in λ is the sum in quadrature of a Poisson term and an additional intrinsic variance term,

$$\mathrm{Var}(\lambda|M) = \frac{1}{\langle \lambda|M \rangle} + \sigma^2_{\ln \lambda|M}. \qquad (13)$$

Using the framework of Evrard et al. (2014)[3], we can readily invert this expression to arrive at

$$\mathrm{Var}(\ln M|\lambda) = \frac{\alpha^2}{\langle \lambda|M \rangle} + \alpha^2 \sigma^2_{\ln \lambda|M}. \qquad (14)$$

This suggests that we model the variance in $\ln M$ at fixed richness via

$$\mathrm{Var}(\ln M|\lambda) = \frac{\alpha^2}{\lambda} + \sigma^2_{\ln M|\lambda} \qquad (15)$$

where we have changed the parametrization to match the type of scatter we have measured.

Rozo & Rykoff (2014) and Rozo et al. (2015a) have estimated the scatter in mass at fixed richness by comparing the redMaPPer catalogue to existing X-ray catalogues and to the *Planck* SZ cluster catalogue (Planck Collaboration et al. 2014). We summarize their findings as $\sigma_{\ln M|\lambda} = 0.25 \pm 0.05$. This means that the Poisson term dominates the scatter for our lowest richness bin, while the additional intrinsic scatter in the $M - \lambda$ relation dominates in our upper richness bins. We tested both Gaussian and lognormal scatter models and find no difference in the recovered parameter values for the mass–richness relation. We adopt the lognormal model as our fiducial model as that is the standard in the literature.

We must also weight the cluster models appropriately in the stack. Clusters at different redshifts have different lensing efficiencies for background galaxies at different redshifts, and the background galaxies themselves contribute less information to the lensing signal as they become fainter and harder to measure; also, we measure the lensing signal using physical distances in the plane of the lens, so clusters with a larger angular diameter distance will contribute fewer pairs to the lensing signal for a fixed source number density in angular coordinates. We construct a per-lens weight that is a function of the angular diameter distance to the lens (which accounts for the physical aperture) as well as the average weight applied to background galaxies (Equation 5) for each lens, which accounts for both the source galaxy redshift distribution and for the fact that the average source galaxy shape weight is a function of redshift (due to the size of the measurement error).

---

[3] To address a possible source of confusion, the Evrard et al. (2014) framework uses α to denote the power-law slope of parameters given mass; i.e. to zeroth order, our α, denoting the power-law slope of mass given λ, is the inverse of theirs.

We have corrected our lensing signal for the fact that we have imperfect, biased knowledge of the source photo-zs. This means we should use the true redshift distribution $P(z_s)$, which we take to be the parametric curve of Nakajima et al. (2012), rather than our biased measured distribution, to compute the expected average weights. If we also had perfect knowledge of the source shape weights as a function of true redshift (and not measured photo-z), we would simply compute

$$\langle w_s \rangle(z_l) = \int_0^\infty \mathrm{d}z_s \ P(z_s)\Sigma_{\mathrm{cr}}^{-2}(z_l, z_s)w_{\mathrm{shape}}(z_s). \qquad (16)$$

While we do not have such knowledge, the weight is only a slowly varying function of z_s, with ~ 5 per cent change over the redshift range covered by our source catalogue, so even with our biased photo-zs, a direct measurement of $w_{\mathrm{shape}}(z_s)$ from our catalogue should contribute negligible errors to our final model prediction. We measure the average shape weights in redshift bins j (which we choose to be narrow bins of width 0.01 in redshift) in our catalogue and combine them with the true redshift distribution to obtain

$$\langle w_s \rangle(z_l) = \sum_j \Delta z_S P_{\mathrm{true}}(z_s)\Sigma_{\mathrm{cr}}^{-2}(z_l, z_s)\langle w_{\mathrm{shape}}(z_{s,j}) \rangle. \qquad (17)$$

Finally, once we account for the differing aperture sizes on the sky for lenses at different redshifts, we obtain a per-lens weight of

$$w_l(z_l) = \frac{\langle w_s \rangle(z_l)}{D_A^2(z_l)}, \qquad (18)$$

normalized so the sum of weights over all clusters is 1.

Putting it all together, given clusters m divided into bins n with redshifts z_m and richnesses λ_m, the expectation value for the lensing profile of a cluster stack is

$$\langle \Delta\Sigma(R) \rangle_n = \sum_{m \in n} w(z_m)\Delta\Sigma(R|M_m, c_m, P_{\mathrm{cen}}, R_{\mathrm{mis}}). \qquad (19)$$

When building the model stack, the mass M_m of cluster m is drawn from the probability distribution $P(M|\lambda_m)$ including the aforementioned scatter model. The concentration c_m is then drawn from a distribution with lognormal width 0.14 dex (Wechsler et al. 2006) and a mean set according to the mass–concentration relation of Bhattacharya et al. (2013) computed by the `colossus` package (Diemer & Kravtsov 2015). We allow for an overall amplitude shift of this fiducial relation by a multiplicative constant c_0. We find that including scatter in the mass–concentration relation has a negligible impact on our results, but we include it in accordance to theoretical expectations. For further details and alternative mass–concentration relations, see Appendix A.

4.3 Likelihood Model

We compute the stacked weak lensing signal of redMaPPer clusters in 4 bins of richness λ and 2 redshift bins. The characteristics of the bins are shown in Table 1. For each galaxy cluster, we compute the observed lensing profile $\widehat{\Delta\Sigma}$ as per Eq. (6), as well as the theoretical model $\Delta\Sigma$ as per Eq. (19). In computing our theoretical prediction, the M assigned to each cluster is scattered relative to its expectation value to take into account the scatter in the mass–richness relation. Given our Monte Carlo approach, this is formally equivalent to treating the mass of each individual cluster as a free

parameter, and marginalizing over all these parameters as part of our MCMC. That is, our procedure is equivalent to a Monte Carlo evaluation of the appropriate integral. We truncate the richness measurements at $\lambda = 140$ to avoid introducing a sparsely populated bin of extremely rich galaxy clusters, where the predicted profiles are unstable due to the random realization of the scatter.

With the observed and modeled lensing profiles, we model the likelihood function as a Gaussian $\mathcal{L} \propto \exp(-\frac{1}{2}\chi^2)$ where

$$\chi^2 = \left[\widehat{\Delta\Sigma}(R) - \langle\Delta\Sigma(R)\rangle \right] \mathbf{C}^{-1} \left[\widehat{\Delta\Sigma}(R) - \langle\Delta\Sigma(R)\rangle \right]. \tag{20}$$

The covariance matrix $\mathbf{C}$ is, for this analysis, diagonal, with the diagonal terms computed as the variance on the mean $\Delta\Sigma$ for each bin. As weak lensing is dominated on small scales by the intrinsic shape distribution of galaxies ("shape noise"), with each source contributing for one lens on average, covariances between bins are typically very small. Jackknife error bars are usually used to estimate this effect, but for these scales, the noise in the jackknife is significantly larger than the expected value of the off-diagonal terms and has a detectable impact even on the diagonal terms, so we use the variance on the mean directly. Based on previous work with this SDSS shape catalogue, we expect this approximation to work well for $R < 5$ Mpc, outside our upper limits for our fitting range (Mandelbaum et al. 2013).

We choose our radial range to avoid contamination from nearby large-scale structure (the so-called "two-halo term" of halo modeling) and to avoid problems due to background selection and increased scatter due to low sky area in the inner regions of clusters. We use $0.3\ h^{-1}$ Mpc as the interior radius limit. Mandelbaum et al. (2010) suggest using minimum scales of 15-25 per cent of the virial radius; our lensing-weighted average virial radius, given the parameters we find below, is about $1.3\ h^{-1}$ Mpc, so our lower radius limit corresponds to $\sim R_{\rm vir}/4$. We choose a richness-dependent upper limit of $2.5\,(\lambda/20)^{1/3}\ h^{-1}$ Mpc based on a comparison of halo model predictions to the single-halo measurements from the simulations we will use for validation in Sec. 5.5. We also tested values of the constant in front of the $(\lambda/20)^{1/3}$ factor above ranging from 1 to 7, and found no statistically significant change in the scientific parameters of interest.

Finally, as will be discussed in Sec. 5, we have an overall calibration uncertainty in our $\Delta\Sigma$ values due to possible shear estimation biases and photo-z biases. To marginalize over these effects, we include in our theoretical model a parameter b such that

$$\widehat{\Delta\Sigma_b}(R) = (1+b)\widehat{\Delta\Sigma}(R). \tag{21}$$

We assume that all clusters are equally affected by this systematic, which maximizes the impact of these effects on the amplitude of the mass–richness relation (i.e. all clusters move up and down in unison).

Our final set of seven model parameters includes the scaling relation parameters $\log_{10} M_0$, α, $\sigma_{\ln M|\lambda}$, the miscentring parameters $P_{\rm cen}$ and τ, the multiplicative constant c_0 that rescales the mass–concentration relation of halos relative to our fiducial model, and the overall multiplicative amplitude shift $1 + b$ corresponding to possible systematic errors in the lensing signal measurement. We use informative priors on parameters that are difficult to measure from

the data due to degeneracies ($\sigma_{\ln M|\lambda}$, $P_{\rm cen}$, τ, and b) and implicitly fix one parameter with strong disagreement between the data and the prior due to our belief that the data is incorrect (the redshift evolution of the mass-richness relation). We use the `emcee` package[4] (Foreman-Mackey et al. 2013) to sample our likelihood function with 100 walkers. We discard the first 100 steps of each walker as burn-in steps. Our reported values correspond to the median result of all samples, and our errors correspond to the difference between the median and the 16th or 84th percentiles of the samples.

5 SYSTEMATIC UNCERTAINTIES

5.1 Measurement Systematics

In this section, we consider systematic uncertainties in the measurement process, including shear and photometric redshift systematics, and systematics associated with our estimator for the lensing signal.

The shear catalogue we use was extensively tested in Reyes et al. (2012), with further error characterization in Mandelbaum et al. (2013). Based on that work, taken together, we expect a systematic error budget of 5 per cent on $\Delta\Sigma$ for lenses in this redshift range and our galaxy shape sample, comprising errors from PSF correction, noise bias, selection bias, and photo-z biases. The first three items in that list, which are linked and which all cause errors or biases in shear estimation, were measured in realistic galaxy simulations and were found to contribute 3.5 per cent to this error budget. The remnant of the systematic error is dominated by photo-z biases, as measured by Nakajima et al. (2012) through comparison to spectroscopic samples. Other effects were also considered, including, for example, stellar contamination and shear responsivity errors, but all were found to be subpercent and thus subdominant to the errors mentioned above. Additionally, the calibration of the recovered shears was tested up to an induced shear of 0.1, larger than we expect to find even for the clusters in our most massive bin at a radius of $0.3h^{-1}$ Mpc, so we should not see biases from mismeasured larger shears near the cluster centres. We refer interested readers to Reyes et al. (2012), Mandelbaum et al. (2012), and Mandelbaum et al. (2013) for more information.

In addition to shear and photo-z biases, our recovered cluster masses and concentrations can be affected by magnification and obscuration[5] of the background sky by cluster member galaxies. However, for this SDSS shape sample, the low-redshift redMaPPer clusters we are using, and the range of transverse separations considered here, these effects are negligible, as demonstrated in Simet & Mandelbaum (2015). The slope of the background galaxy population number counts with flux and size, which contribute to the size of the magnification effect (Schmidt et al. 2009), are too shallow to make magnification detectable for this lens sample and range of R. Obscuration effects are large when many of

---

[4] http://dan.iel.fm/emcee/
[5] Here, obscuration refers not only to the literal blocking of source galaxies by member galaxies, but also the inability to properly select them due to blending with member galaxies. This is sometimes called crowding.

the cluster galaxies can be seen (deeper imaging), leading to portions of the background sky being unobservable either directly or through blending. Again, this is less pronounced in SDSS than in deeper surveys. We measure number densities to determine the obscuration area of the redMaPPer member galaxies, and rerun the fitting code from Simet & Mandelbaum 2015 for our much larger radius range. We find sub-percent biases in our final mass determinations. Consequently, we ignore magnification and obscuration as sources of systematic uncertainty in our measurements.

As a further test for systematic errors due to observational effects such as shear and photometric redshift estimation, we compare our measurements to those from a fully independent shear and photo-z catalogue. The catalogue, which we will refer to as the ESS catalogue, has been used in a number of other lensing studies (e.g., Melchior et al. 2014; Clampitt & Jain 2015). The shapes in the ESS catalogue were also measured using the re-Gaussianization technique, but the code was developed independently. The code used to generate the catalogue is freely available online[6]. The ESS catalogue also makes use of the photo-zs released by Sheldon et al. (2012). The full photometric redshift probability distributions $p(z)$ were used to calculate the $\Delta\Sigma$ for each lens-source pair. $\Delta\Sigma$ was measured using the publicly available `xshear`.[7]

Because the same re-Gaussianization PSF-correction algorithm was used for both our primary catalogue and the ESS catalogue, we may expect the catalogues to have the same overall shear calibration. However, it is still useful to compare these catalogues. First, there could be real differences in the implementation of the re-Gaussianization algorithm, resulting in small differences in the final shear calibration. Second, differences in the photo-z generation and use of the full $p(z)$, rather than the point estimates with correction for resultant biases, could result in different overall normalization for $\Delta\Sigma$ if done inconsistently. Third, although the same data were used as input for both codes, how the data were used and organized, and the galaxy selection criteria, differs in detail. Fourth, there could be software "bugs" that could result in inconsistent lensing results between the catalogues.

We show the signal for redMaPPer clusters with redshifts $0.1 - 0.3$ and richnesses $\lambda = 20 - 203$ in Figure 1. We compare the radial scales $500h^{-1}$ kpc to $10h^{-1}$ Mpc. The lower edge is set by the presence of selection effects in the ESS catalogue that lead to scale-dependent suppression of the lensing signal. We note that these selection effects were known *a priori*, but that no attempt was made to correct for these since the goal of this test is simply to compare the $\Delta\Sigma$ calibrations of the two independent shear and photo-z pipelines in the regime where selection effects are unimportant. The upper limit of the scales used in our tests is set by the maximum radius considered in this work. We test for consistency between the two shape and photometric redshift catalogues by minimizing $\chi^2 = \sum[\Delta\Sigma' - (1+a)\Delta\Sigma]^2/\sigma^2_{\Delta\Sigma}$ for some constant a. We find $a = 0.031 \pm 0.033$, largely insensitive to the magnitude of the correlations between the two $\Delta\Sigma$ estimators, and also insensitive to the exact end
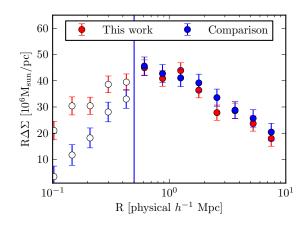
[6] https://github.com/esheldon/admom
[7] https://github.com/esheldon/xshear

Figure 1. Lensing signal from the redMaPPer catalogue for our analysis ("this work") and the comparison ESS catalogue ("comparison"). We consider the signals comparable at all scales $\geqslant 500h^{-1}$ kpc. Filled circles are comparable data points, while open circles are shown for scales smaller than the cutoff.

points used for the comparison as long as we are above the $500h^{-1}$ kpc cutoff. Thus we can exclude any significant relative differences in calibration of $\Delta\Sigma$ between these two independently-produced catalogues, in line with our expectations of $\lesssim 5$ per cent multiplicative bias as detailed above.

In our work, we have corrected for dilution of the source sample by cluster member galaxies under the assumption that cluster member galaxies have zero shear. If cluster member galaxies are radially aligned, however, our correction will be underestimated. Blazek et al. (2012) tried to measure the radial intrinsic alignment (IA) signal of galaxies in our source sample with respect to the positions of Luminous Red Galaxies (LRGs) at a similar redshift to our clusters. They were unable to detect an intrinsic alignment signal, placing an upper limit of 1.5% on the fractional contamination of intrinsic alignments on the recovered galaxy-galaxy lensing signal at a separation of $1h^{-1}$Mpc. To estimate an upper limit for this work, we must consider two factors: differences in the intrinsic alignment strength, and differences in the $\Delta\Sigma$ (which will modify the fractional contamination estimate). To estimate the former, we use the fact that the intrinsic alignment strength depends on the type and luminosity of the source galaxies (which is the same in this work and that one), and on the density tracers used as lenses. Singh et al. (2015) provides an empirically-determined power-law relationship between the small-scale intrinsic alignment strength and the halo mass of the density tracer, which we can use to scale up the estimated intrinsic alignment. After taking into account the increase in lensing signal $\Delta\Sigma$ between our clusters and LRGs, we find that the 1.5% upper limit on fractional contamination for LRG lenses corresponds to an $\approx 6\%$ upper limit for galaxy clusters. While this upper limit is comparable to our uncertainties, we note that IA remains undetected for typical satellite galaxy populations in galaxy clusters (e.g., Sifón et al. 2015), with detections only for LRGs (e.g., Singh et al. 2015). For the purposes of this work, we have chosen not to increase our systematic error budget, pending future investigations of intrinsic alignments in galaxy clusters. Indeed, these ar-

External Data Set	Number	f	τ
XCS	82	0.85 ± 0.05	0.48 ± 0.09
ACCEPT	54	0.75 ± 0.06	0.31 ± 0.05

Table 2. Constraints on the miscentring parameters from each of the various external data sets. The "number" column refers to the total number of clusters in the sample. The parameter f is the fraction of miscentred clusters; the parameter τ characterizes the width of the centring offset distribution of miscentred clusters.

guments suggest that IA may soon become an important systematics that must be simultaneously fit for when analyzing stacked cluster lensing data (unless all galaxies at or very near the cluster redshift can be robustly removed).

5.2 Cluster Miscentring

Some fraction of the redMaPPer clusters are expected to be miscentred. Based on the redMaPPer miscentring probabilities, we expect 87% of the galaxy clusters to be correctly centred. This value is consistent with the fraction of clusters for which the X-ray centre of the galaxy cluster is in close proximity to the central galaxy assigned by redMaPPer (Rozo & Rykoff 2014). Here, we further characterize the miscentring scale τ that governs the radial offset of miscentred clusters. Specifically, we compute the distribution of positional offsets R of galaxy clusters shared between redMaPPer and two high-resolution X-ray external data sets, the XCS DR1 (Mehrtens et al. 2012) and ACCEPT (Cavagnolo et al. 2009) cluster catalogues. The distributions are modeled as

$$P(R) = \frac{f}{R_0} \exp(-R/R_0) + (1-f)\frac{R}{\tau^2 R_\lambda^2} \exp\left(-\frac{1}{2}\frac{R^2}{\tau^2 R_\lambda^2}\right).$$
(22)

This distribution has 3 free parameters: the fraction of clusters that are correctly centred f, the parameter τ governing the centring offset distribution of miscentred clusters, and the parameter R_0 describing the centring offset between the external data set and redMaPPer clusters for correctly centred clusters. Note that correctly centred clusters will still have offsets relative to external data sets due to both centring uncertainties in the external data set and physical displacements between the location of the central galaxy and the centre of the intra-cluster gas. The parameter R_0 accounts for these displacements. It is usually small—such offsets tend to peak at $\lesssim 0.1$ Mpc (Cui et al. 2016a). As R_0 models an offset in the X-ray detection relative to the dark matter halo, which is not relevant for our optical centring measurements here, we do not include it in our model width. Additionally, since the parameter itself is smaller than our uncertainty on our prior, any errors in R_0 should already be reflected in our modeling.

The likelihood of each of the combined data sets (XCS and ACCEPT) is the product of the probability $P(R)$ over the clusters in the joint cluster samples. The resulting constraints are summarized in Table 2, where we report the mean and standard deviation of the parameters computed from the MCMC. We do not report on the posterior of the parameter R_0 since it is purely a nuisance parameter for this study.

From Table 2, we see that the two high-resolution X-ray data sets are consistent with each other and with our ex-

pectation $f = 87\%$. We consider two analyses: one in which the miscentring priors are chosen following a "middle-of-the-road" approach, with a gaussian prior $f = 0.80 \pm 0.07$ and $\tau = 0.40 \pm 0.1$, and one for which the miscentring fraction is set to the expected value $f = 0.87$ based on the redMaPPer centring probabilities. We note that from the summary of our binning scheme in Table 1 one can see that the reported fraction f from the redMaPPer algorithm itself is roughly constant for all λ and redshift bins, so we do not include further richness or redshift evolution in this parameterization beyond what is implied by the dependence of miscentring radius on the cluster radius.

5.3 Cluster Projections

Photometric cluster finding is known to suffer from projection effects. That is, two neighboring clusters that fall along the line of sight will be blended by the photometric cluster finder into a single, apparently larger cluster. We estimate the projection rate in the redMaPPer cluster catalogue to be $p = 10 \pm 4$ per cent (see Appendix C). Characterizing the impact of such projections on cluster mass calibration is not trivial, but rough scalings can be readily estimated. In particular, clusters that appear in projection will also have a lensing signal affected by said projection effects. If the richness λ scales roughly linearly with the mass M, then the total projected mass per unit richness will remain constant, implying that projected clusters simply slide up and down the richness mass relation, without deviating from it. Indeed, this effect has been seen in numerical simulations (Angulo et al. 2012; Noh & Cohn 2012). Below, we quantify this effect in a way that can be incorporated into our analysis.

Consider a projection of two halos of mass M and richness λ which are blended into a single cluster of richness 2λ. Assuming $M \propto \lambda$, a clean cluster of richness 2λ would have a mass $2M$. By contrast, the blended cluster will appear to have a mass $(1 + \epsilon)M$, where ϵ characterizes the effective mass contribution of the projected halo. This effective mass will depend on the relative position of the two blended halos along the line-of-sight, the concentrations of the two halos, etc., but we will treat ϵ as a single effective parameter that characterizes all of these effects. Letting $\langle M \rangle_0$ be the mass of galaxy clusters of a given richness in the absence of projection effects, and p be the fraction of projected clusters, then the observed weak lensing mass of a cluster stack will take the form

$$\langle M \rangle = (1-p)\langle M \rangle_0 + p(0.5 + \epsilon)\langle M \rangle_0$$
(23)

Note that projected halos will only contribute their full mass ($\epsilon = 1/2$) if they are perfectly aligned, and will never contribute no mass ($\epsilon = 0$). We generously set $\epsilon = 0.25 \pm 0.15$, which encompasses the two previously mentioned extremes at less than 2σ. Solving for $\langle M \rangle_0$, we finally arrive at

$$\frac{\langle M \rangle_0}{\langle M \rangle} = \frac{1}{1 + p(\epsilon - 0.5)} = 1.02 \pm 0.02.$$
(24)

The uncertainty ± 0.02 was estimated by randomly drawing both the fraction of projected clusters $p = 0.10 \pm 0.04$, and the parameter $\epsilon = 0.25 \pm 0.15$. We computed the ratio $\langle M \rangle_0 / \langle M \rangle$ for each realization, and repeated 10^4 times to estimate the corresponding variance in the correction factor.

5.4 Cluster Triaxiality

Dark matter halos are known to be triaxial. Optically selected halos are expected to be biased so that they are preferentially elongated along the line of sight. In this case, the galaxy contrast relative to the immediate neighborhood should be maximized, making cluster detection easier. The elongation of the halo along the line of sight will naturally lead to an enhanced weak lensing signal, and so the recovered mass–richness relation may well be affected by this type of selection effect. For our purposes, the key point is that cluster triaxiality induces covariance between cluster richness and weak lensing mass estimates.

The magnitude of this type of selection effect can be readily estimated using the multi-model cluster component of Evrard et al. (2014). If $\langle M \rangle_0$ is the halo mass in the absence of triaxiality-induced selection effects, and $\langle M \rangle$ is the recovered weak lensing mass, then one has

$$\frac{\langle M \rangle_0}{\langle M \rangle} = \exp\left[-\beta r \sigma_{\ln M|\lambda} \sigma_{\ln M|WL}\right] \qquad (25)$$

where β is the slope of the halo mass function at the relevant scale, r is the correlation coefficient, and $\sigma_{\ln M|\lambda}$ and $\sigma_{\ln M|WL}$ is the scatter in mass at fixed richness and weak lensing mass respectively. Using the simulation results of Noh & Cohn (2012), we find $r = 0.25$. We do not have an uncertainty estimate for this correlation coefficient, so we adopt a prior $r \in [0, 0.5]$. We set $\sigma_{\ln M|WL} = 0.25 \pm 0.05$ based on the results by Becker & Kravtsov (2011), and $\sigma_{\ln M|\lambda} = 0.25 \pm 0.05$ as discussed earlier. We use a Monte Carlo approach in which all of the above quantities are randomly drawn in order to estimate the final correction and its uncertainty. We arrive at

$$\frac{\langle M \rangle_0}{\langle M \rangle} = 0.96 \pm 0.02 \qquad (26)$$

That is, weak lensing masses overestimate the true mass of photometrically selected clusters by $4\% \pm 2\%$. This value is in excellent agreement with the simulation-based estimates of Dietrich et al. (2014).

The combined effects of cluster projections and cluster triaxiality can be summarized as

$$\frac{\langle M \rangle_0}{\langle M \rangle} = 0.98 \pm 0.03 \qquad (27)$$

We apply this multiplicative correction to our recovered best-fit amplitude of the mass–richness relation *a posteriori*, and add in quadrature the above 3% systematic uncertainty to our total systematic error budget.

5.5 Modeling Systematics

Recent work indicates that the more flexible Einasto profile (3 free parameters; Einasto 1965; Dutton & Macciò 2014) may describe dark matter halos more accurately than our assumed NFW profile. Depending on the details of the weak lensing analysis, the differences between Einasto and NFW profiles can be significant. For instance, Sereno et al. (2016) find biases from fitting NFW profiles to Einasto halos that range from -1% for low- and middling-mass clusters to $\sim +15\%$ for the highest-mass clusters. However, these biases come from fits that use smaller radii (by a roughly a factor of two) than the smallest radial bin considered in

this study. The biases we see should be less, since the difference between NFW and Einasto profiles is largest at small scales; Mandelbaum et al. (2008a) performed fits over a radius range more similar to ours and found negligible differences in the masses and moderate differences in the concentrations. Therefore, we do not expect to see such large biases because of the modest range of scales we probe. Nevertheless, the main point stands: one should check whether the profile assumed induces a significant bias in the weak lensing mass estimate. This is especially true in our case, since we rely on an NFW halo out to scales comparable to the splashback radii of our halos, where one expects systematic deviations from the NFW profile (Diemer & Kravtsov 2014).

Here, we address this source of systematic uncertainty using numerical simulations to test whether our parametric models can introduce significant biases in our recovered weak lensing masses. Specifically, we use an N-body simulation with a volume $V = [1.05 \ h^{-1} \ \mathrm{Gpc}]^3$ and 2.7 billion particles, run with the L-Gadget code, a variant of Gadget (Springel 2005). The cosmological model is flat ΛCDM with matter density $\Omega_m = 0.318$, $\sigma_8 = 0.835$, and $h = 0.670$, and $n_s = 0.961$. We use the halo catalogue generated by the Rockstar halo finder (Behroozi et al. 2013). In this simulation a $3.5 \times 10^{13} \ h^{-1} M_\odot$ halo is resolved with 10^3 particles.

We construct synthetic weak lensing profiles from the numerical simulation. First, we divide the simulation into 64 jackknife regions. We assign an observed "richness" to each halo in the simulation via $\lambda = M_{\mathrm{obs}}/10^{14} h^{-1} M_\odot$. M_{obs} is the effective observed mass of the halo, computed via $\ln M_{\mathrm{obs}} = \ln M_{\mathrm{true}} + \delta$ where δ is a Gaussian random draw of zero mean and variance $\langle \delta^2 \rangle^{1/2} = 0.2$, intended to model lognormal scatter in the mass–observable relation. Clusters are sorted into richness bins, and the lensing profiles for these bins are fit using our likelihood model with no miscentring. We change the Ω_m of our model-fitting pipeline to the value from the simulations for these tests only. We adopt the same mass–richness relation model as Eq. (12), this time with pivot $\lambda = 1$, and we allow for lognormal scatter in mass at fixed richness. We use the data error bars to replicate our sensitivity to different radius scales, and combine the results from the 64 jackknife samples to measure any potential bias at a higher precision than the data error bars would allow from any one fitting procedure alone.

Using the formalism in Evrard et al. (2014), the resulting best fit M_0 value should be $\log M_0 = 14.0 - \beta \sigma_{M|\lambda}^2 / \ln(10) = 13.953 \pm 0.006$, where β is the slope of the halo mass function over the range of halo masses probed. The error bar in our theoretical predictions comes from the difference between the first and second-order calculation using the formalism of Evrard et al. (2014). We compare this expectation against our recovered M_0 values to characterize the systematic uncertainty $\Delta \log M_0$ associated with our parametric modeling. We find results consistent with our expected value, 13.953 ± 0.001 if we use all simulation mass bins or 13.943 ± 0.004 if we use only the bins within our expected observational mass range. As the error bar is dominated by the theoretical uncertainty, we choose to add no further uncertainty to our error budget based on this comparison.

5.6 Baryonic effects

Baryonic physics may modify the matter density profile of halos relative to that observed in dark matter-only simulations. Simulations that include baryonic cooling as well as AGN feedback have been used to study the impact of baryons on halo profiles (e.g., Schaller et al. 2015; Cui et al. 2016b; Bocquet et al. 2016). We summarize the trends in these papers as follows. First, on very small scales, the stellar mass component of the central galaxy dominates. These scales are excluded from our analysis. At somewhat larger scales, the profiles become either more or less concentrated depending on the relative impact of baryonic cooling to AGN feedback. The halos are still roughly NFW, but the scale radius r_s changes, reflecting the overall mass redistribution within a halo. The fact that we marginalize over a rescaling of the concentration–mass relation should allow us to avoid substantial biases in mass estimates due to the change in halo concentrations. Third, and most importantly for our purposes, the mass within R_{200m} is very stable, well below the 5% level. As such, we expect the impact of baryons is well below our final error budget, and is therefore ignorable. Nevertheless, we caution that the impact that baryonic physics has on M_{200m} is likely to become relevant to future weak lensing experiments. Fortunately, a straightforward generalization of the calibration program detailed above relying on simulations with baryonic physics should easily allow us to incorporate such systematics in future analyses.

5.7 Systematics Summary

The systematics we consider are: shear and source photometric redshift systematics ($\pm 5\%$ in $\Delta\Sigma$), cluster projections, halo triaxiality (combined $-2 \pm 3\%$ in M_0), and modeling systematics (no additional uncertainty). We handle the $\Delta\Sigma$ errors via marginalizing over the fitting parameter b as described in Section 4.3; we note that this is a 5 per cent tophat prior, which when combined with other Gaussian errors should contribute approximately 3.5 per cent to a Gaussian uncertainty on the overall amplitude. We apply the errors and bias correction in M_0 due to halo triaxiality and halo projections *a posteriori* to our measured mass amplitude from our fitting procedure.

In the previous sections, we specified miscentring priors, but we did not estimate how miscentring impacted the uncertainty in the recovered weak lensing mass. To test this, we compare the results of our fiducial analysis to a second analysis in which the miscentring parameters are held fixed at their fiducial values. We find the resulting uncertainties in the amplitude of the mass–richness relation are essentially identical, so cluster miscentring does not appear to have a significant impact on the precision of weak lensing mass calibration. It does, however, impact the uncertainties in concentration. In short, current miscentring estimates are sufficiently accurate to be negligible for mass calibration purposes, but not for analyses of the mass–concentration relation.

Since we have included our systematic uncertainties in the outputs of the MCMC chains themselves, we cannot distinguish systematic from statistical errors in this calculation. To obtain a statistical error, we run a separate chain with all the nuisance parameters (b, the miscentring parameters,

and our bias correction) fixed to their central values, with no uncertainty included, and measure the statistical error from the uncertainty in the resulting parameters. We subtract this in quadrature from the total systematic plus statistical uncertainty to obtain the systematic uncertainty.

6 RESULTS

Figure 2 shows the results from our MCMC fitting procedure. We obtain a fit with $-2\ln\mathcal{L} = 76.37$, which would (without our priors) correspond to a χ^2 value for 72 degrees of freedom. That is, our model is a good fit to the data. A sampling of the models from our chains along with our data can be seen in Figure 3. Table 3 reports our model parameters, along with the corresponding priors and posteriors. We note that the amplitude and slope of the mass–richness scaling relation, as well as the amplitude of the mass–concentration relation, are tightly constrained. Our constraint on the amplitude of mass–richness relation parameter is $\log M_0 = 14.344 \pm 0.021$ (statistical) ± 0.023 (systematic), corresponding to a 7% calibration of the amplitude of the scaling relation. The corresponding constraint on the power-law index of the mass-λ relation is $\alpha = 1.33^{+0.09}_{-0.10}$. The posterior probability for the scatter in the mass–richness relation and the miscentring probability is largely unchanged from the input priors, demonstrating that the external data sets utilized to derive the priors are significantly more sensitive to these parameters than the stacked weak lensing signal measured in this work.

There is a degeneracy between P_{cen} and the amplitude of the mass–concentration relation, which is unsurprising, as both parameters correspond to shifts in the "peakiness" of the profile. τ is not included in this degeneracy, but shifts in τ have a smaller effect on the profile since P_{cen} is large.

We do not show the parameters $\sigma_{\ln M|\lambda}$ or b, which are unconstrained by the data. $\sigma_{\ln M|\lambda}$ is not degenerate with any other parameter, and we find no preference for any value within our tophat prior range. We also find no preference for any value of b. Not surprisingly, we find that b is degenerate with the mass, with the mass scaling as $10^{-b/2}$ for our fits. Also, b is degenerate with the concentration amplitude c_0, with $c_0 \propto 1 - b$.

In Fig. 4, we show how our fitted mass–concentration relation compares to two theoretical models, Bhattacharya et al. (2013) and Diemer & Kravtsov (2015). We also show the mass–concentration relation recovered when we fix P_{cen} to the value expected from the redMaPPer catalogue, 0.87. In both cases, we find somewhat higher values of c than the theoretical models predict, but the difference is only 1σ and hence not statistically significant. Appendix B also demonstrates that allowing for redshift evolution in the mass–richness relation does not alter any of our conclusions. In Appendix A we show results with and without various complicating factors (such as miscentring and a variable mass–concentration relation), to aid comparison with other works and to show the effects of those factors for interested readers.

Because the halo mass definition is dependent on cosmology, our results change if we alter Ω_m. We perform the same analysis as above with Ω_m from $0.26 - 0.34$ to check the dependence of our parameters on cosmology, altering Ω_Λ as well to maintain a flat universe. Only the mass am-
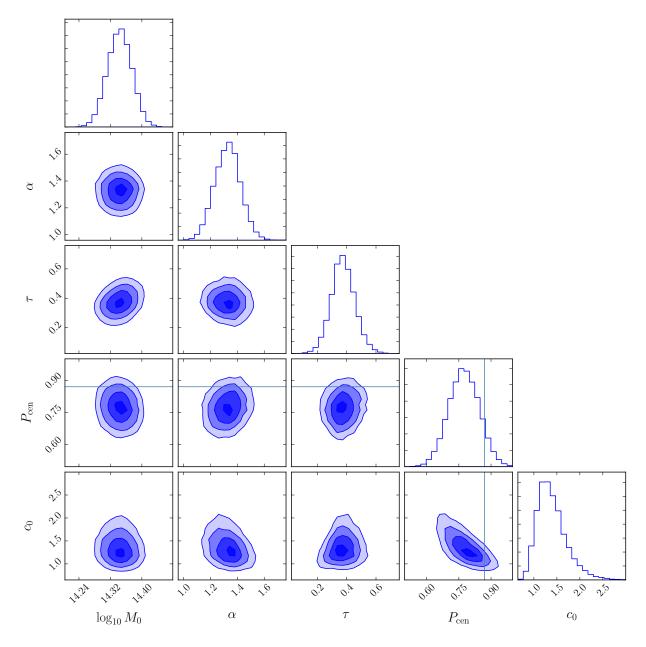
Figure 2. Results from our MCMC model fitting. Contours indicate the 0.5, 1, 1.5, and 2σ levels, and the 1 dimensional histograms are shown on the diagonal. The range shown for each parameter does not necessarily correspond to the top-hat prior ranges. Parameters and priors are described in Table 3. The solid line denotes the expected value of $\langle P_{\rm cen} \rangle = 0.87$ from the redMaPPer catalogue.

plitude changes, as expected; we find that $\log_{10} M_0$ is linear with Ω_m near $\Omega_m = 0.3$, with the scaling $\log_{10} M_0 = 14.344 - 0.706(\Omega_m - 0.3)$. As expected, M_0 decreases as Ω_m increases.

7 DISCUSSION

We compare our results to a variety of constraints from the literature. The first mass–richness relation for redMaP-Per clusters was a rough abundance-matching estimate presented in Rykoff et al. (2012), who suggested a scaling relation with $\alpha = 1.08$ and $M = (3.9 \pm 1.2) \times 10^{14} \ h^{-1} \ M_\odot$

at $\lambda = 60$, in excellent agreement with our recovered value of $(3.7 \pm 0.3) \times 10^{14} \ h^{-1} \ M_\odot$. There is an apparent slight tension (2.5σ) in the value of the slope, but Rykoff et al. (2012) did not report an uncertainty in the slope. We note that Rykoff et al. (2012) emphasized their reported relation was only meant to be a place holder for subsequent mass calibration efforts such as this one.

Miyatake et al. (2016) used the same SDSS weak lensing shear catalogue and photo-z catalogue and calibration as we did to constrain the mean mass of entire redMaPPer cluster catalogue. Despite the shared input data set, there are significant methodological differences between the two analyses. In particular, our science goal led us to provide a
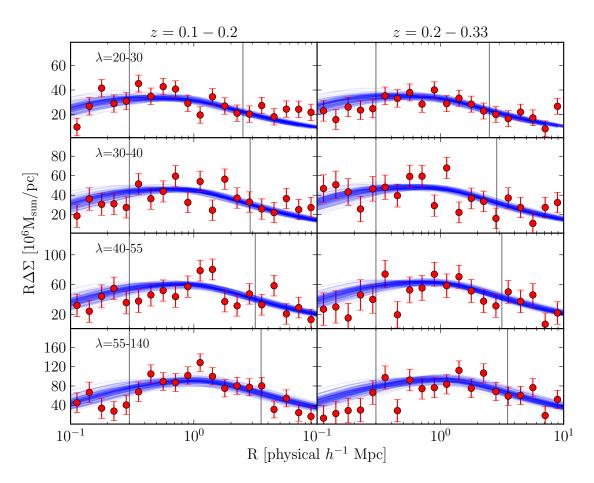
Figure 3. Lensing signal ($R\Delta\Sigma$) from the redMaPPer catalogue for the eight bins described in Table 1, plus a sampling of models from the MCMC chain. The fit was performed only to data points lying between the vertical lines.

Parameter	Description	Prior	Median and error (posterior)	Median and error ($P_{cen} = 0.87$)
$\log_{10} M_0$	Log amplitude of scaling relation at $\lambda_0 = 40$ in units of $h^{-1}M_\odot$, with definition M_{200m}	(13, 15)	$14.344 \pm 0.021 \pm 0.023$	$14.338 \pm 0.021 \pm 0.021$
α	Power-law index of dependence on λ	(0, 2)	$1.33^{+0.09}_{-0.10}$	1.34 ± 0.09
$\sigma_{\ln M \vert \lambda}$	Intrinsic scatter of $\lambda - M$ relation	(0.2, 0.3)	0.25 ± 0.03†	0.25 ± 0.03†
c_0	Amplitude of mass–concentration relation as a multiple of Bhattacharya et al. (2013)	[0, 3]	$1.34^{+0.35}_{-0.25}$	$1.11^{+0.16}_{-0.14}$
τ	Width of the Gaussian miscentring distribution	$\mathcal{N}(0.4, 0.1)$	0.37 ± 0.08†	0.38 ± 0.09†
P_{cen}	Fraction of clusters with correct centres	$\mathcal{N}(0.80, 0.07)$	0.77 ± 0.07†	—
b	Multiplicative amplitude shift to accommodate systematic errors in $\Delta\Sigma$	(-0.05, 0.05)	0.00 ± 0.03†	0.00 ± 0.03†

Table 3. Parameters from Eqs. (12) and (19), a short description of the meaning, the prior, and the median of all MCMC samples plus the errors given by the 16th and 84th percentiles of the samples. M_0 has been corrected from the output of the MCMC chain for model bias, as described in Section 5. We also show the results if we fix P_{cen} to 0.87, the mean value from the redMaPPer catalogue centring probabilities. A range means a tophat prior; $\mathcal{N}(x, \sigma)$ is a Gaussian prior with mean x and width σ. For posteriors with two uncertainties given, the first is statistical and the second is systematic. The † symbol indicates values that are largely determined by our priors rather than our data.

much more detailed systematics analysis than that presented in Miyatake et al. (2016). The end mass calibrations are, perhaps not surprisingly, very similar. Our principal contribution is the quantitative characterization of the systematic uncertainties inherent to this measurement, as well as determination of the scaling of mass with λ instead of just a population average.

Li et al. (2016) produced a weak lensing calibration of the mass–richness relation as a by-product of their analysis on the lensing profile of cluster substructures. Specifically, they assume a mass–richness relation that was identical to
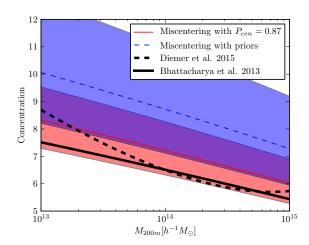
Figure 4. The mass–concentration relations of Bhattacharya et al. (2013) and Diemer & Kravtsov (2015), both at redshift $z = 0.2$, along with the 1σ confidence intervals for our $M - c$ relation with fitted amplitude, both with free miscentring and with $P_{\rm cen}$ fixed to its value from the redMaPPer catalogue.

that of Rykoff et al. (2012), except modulated by an amplitude A. This amplitude is allowed to float when considering substructures in different radial bins. We combine the various radial bins, ignoring the innermost bin because it is discrepant with the rest of the data, and is the bin most likely to be affected by systematic uncertainties from magnification, non-weak shear, and source obscuration. Averaging the Li et al. (2016) data results in $A = 0.803 \pm 0.016$, corresponding to $M = (2.09 \pm 0.04) \times 10^{14} \ h^{-1} \ M_\odot$ at $\lambda = 40$. This value is in excellent agreement with our recovered value of $M = (2.21 \pm 0.15) \times 10^{14} \ h^{-1} \ M_\odot$. We note the error quoted in Li et al. (2016) is statistical only.

Recent work by Farahi et al. (2016) has calibrated the mass–richness relation of redMaPPer clusters using stacked velocity dispersion information. They report $M_{200c} = (1.56 \pm 0.35) \times 10^{14} \ M_\odot$ at $\lambda = 30$ with $h = 0.7$. This can be compared to our prediction $M_{200c} = (1.60 \pm 0.11) \times 10^{14} \ M_\odot$, in excellent agreement with their result. The corresponding slopes are also in excellent agreement, $\alpha = 1.33^{+0.09}_{-0.10}$ in our analysis, and $\alpha = 1.31 \pm 0.14$ in theirs.

Saro et al. (2015, hereafter referred to simply as Saro) calibrated the richness–mass relation for redMaPPer clusters in the Dark Energy Survey Science (DES) Verification data by cross-matching DES redMaPPer clusters to clusters found by the South Pole Telescope (SPT Bleem et al. 2015). The SPT clusters were assigned masses by assuming the SPT cluster abundance is consistent with a flat ΛCDM cosmology with $\Omega_m = 0.3$ and $\sigma_8 = 0.8$. In this way, the SPT clusters are assigned both a mass — for which they utilized M_{500c} — and a richness, allowing Saro et al. (2015) to infer the cluster richness–mass relation. Using the framework of Evrard et al. (2014), the corresponding mass–richness relation can be written as $\langle M_{500c}|\lambda \rangle = (3.2 \pm 0.6) \times 10^{14} \ h^{-1} \ M_\odot$ at $\lambda = 66.1$, the pivot richness for their sample. The above value is corrected for the predicted redshift evolution between the Saro redshift pivot point and ours, using the Saro constraints on the evolution of the mass–richness relation, and the corresponding uncertainty has been adequately

propagated. We convert our predicted masses from M_{200m} to M_{500c} following Hu & Kravtsov (2003) and the Bhattacharya et al. (2013) mass–concentration relation to arrive at a predicted mass $M_{500c} = (2.2 \pm 0.15) \times 10^{14} \ h^{-1} \ M_\odot$, in reasonable agreement (1.6σ) with the Saro value. Despite the apparent disparity in the central values for the slopes of the mass–richness relation — Saro finds $\alpha = 0.91 \pm 0.18$, compared to our value $1.33^{+0.09}_{-0.10}$ — the two values are consistent at the 2σ level. We note that the above comparison assumes there is no systematic offset in the richness measurements of a galaxy cluster between the SDSS and DES data sets, an assumption that is currently not testable. Indeed, the agreement between the two measurements could be interpreted as evidence that there are no large systematic differences in the richness between the two data sets, as suggested by a comparison of their relative abundances (Rykoff et al. 2016).

Our miscentring values are largely controlled by our priors, as we do not have as much constraining power with the weak lensing only due to degeneracies between parameters that modify the profile shape. We can compare these miscentring parameters to previous results as well. Our lensing-weighted average R_λ is 0.79, so our miscentring τ corresponds to approximately $R_{\rm mis} = 0.29 \pm 0.06 h^{-1}$ Mpc. Rozo & Rykoff (2014) find offsets corresponding to constant probability out to $R_{\rm mis} = 0.8 h^{-1}$ Mpc. However, we note that their straight-line fit is in fact similar to the cumulative distribution function of the Rayleigh distribution we assume for our miscentring offsets. The constant probability out to $R_{\rm mis} = 0.8 h^{-1}$ Mpc that they find is approximately equivalent to a Rayleigh distribution with $R_{\rm mis} = 0.3 h^{-1}$ Mpc, very consistent with our results. Our peak value is smaller than the simulations of the MaxBCG cluster sample (Johnston et al. 2007a) of $\sim 0.4 h^{-1}$ Mpc, although as that catalogue uses different methods of finding the centre of a galaxy clusters, discrepancies should be expected. The RCS cluster sample has a well-measured miscentering width of $0.41 \pm 0.01 h^{-1}$ Mpc for $10^{14} M_\odot$ halos (van Uitert et al. 2016), in good agreement with our measurement of $0.43 \pm 0.09 h^{-1}$ Mpc for the same halos. Their fraction of correctly-centred halos is smaller, again reflecting differences in the cluster-finding algorithms or perhaps differences in the performance of the centroiding algorithm with redshift, as they include clusters up to $z = 0.7$.

As for the mass–concentration relation, our results appear to be in excellent agreement with theoretical expectations. We caution, however, that we while our model account for projection effects, halo triaxiality, and cluster miscentring with regards to calibrating the mass–richness relation, we have not performed a similar calibration for the impact on concentration. Indeed, a recent paper by Baxter et al (in prep), looking at the clustering of redMaPPer clusters, demonstrated that redMaPPer clusters tend to be preferentially more compact than randomly oriented halos, an effect which would tend to bias our recovered parameter c_0 to values larger than unity, exactly as observed. We postpone a detailed calibration of this effect, and therefore a more detailed comparison to numerical simulations and observational studies, to future work.

8 SUMMARY

We have measured the weak lensing signal around 5,570 clusters in the redMaPPer catalogue from SDSS DR8, with richnesses $20 < \lambda < 140$ and redshifts $0.1 < z < 0.33$. The signal shows good agreement with a comparison signal calculated using the same cluster catalogue, but a different shape measurement pipeline and photo-z algorithm and pipeline.

The mass modeling method we use is an extension of previous work, such as the maximum-likelihood lensing approach adopted by Han et al. (2015) and the combination fits of Ford et al. (2014). The model makes it easy to self-consistently include a varying mass–concentration relation and scatter in the mass–richness and mass–concentration relations, as well as removing uncertainty from the question of which richness in a richness bin best corresponds to the mass value obtained from a single-halo fit. We test the model on N-body simulations and find excellent agreement with the true input cluster sample properties.

We fit a parameterized model for the mass–richness relation to the lensing signal, allowing the mass–concentration relation to float to obtain a good fit, accounting for cluster miscentring and scatter in the mass–richness relation, and marginalizing over remaining multiplicative errors in our lensing measurement. We find a mass–richness relation of

$$\langle M_{200m}|\lambda \rangle = 10^{14.344 \pm 0.021 \text{ stat.} \pm 0.023 \text{ sys.}} \left(\frac{\lambda}{40} \right)^{1.33^{+0.09}_{-0.10}} \tag{28}$$

which is consistent with previous measurements using lensing, and in modest agreement with results from the SZ effect.

Including miscentring and a varying mass–concentration relation are important to obtaining accurate results with this sample in this radius range. That is, while our priors on cluster centring are sufficiently tight that miscentring does not contribute a significant fraction of the variance in our mass calibration, we find that ignoring centring outright would result in a 0.3σ systematic shift in the slope of our mass–richness relation towards higher values.

The results in this work provide the most careful weak lensing mass calibration analysis of the redMaPPer cluster catalogue to date, with a detailed budget of systematic uncertainties and null tests. This is also the first time that a cluster mass calibration effort has included a null test comparing two independently developed photo-z and shear codes as a way to validate the estimated systematic uncertainties in the recovered halo masses. Our results provide a critical stepping stone towards placing cosmological constraints with the redMaPPer cluster sample, and pave the way for similar analyses in upcoming photometric survey data, such as that of the DES, HSC, and LSST surveys.

REFERENCES

Abazajian K., Dodelson S., 2003, Physical Review Letters, 91, 041301
Aihara H., et al., 2011, ApJS, 193, 29
Albrecht A., et al., 2006, ArXiv Astrophysics e-prints,
Allen S. W., Evrard A. E., Mantz A. B., 2011, ARA&A, 49, 409
Angulo R. E., Springel V., White S. D. M., Jenkins A., Baugh C. M., Frenk C. S., 2012, MNRAS, 426, 2046
Bacon D. J., Refregier A. R., Ellis R. S., 2000, MNRAS, 318, 625
Bartelmann M., 1996, A&A, 313, 697
Bartelmann M., Schneider P., 2001, Phys. Rep., 340, 291
Becker M. R., Kravtsov A. V., 2011, ApJ, 740, 25
Becker M. R., et al., 2016, Phys. Rev. D, 94, 022002
Behroozi P. S., Wechsler R. H., Wu H.-Y., 2013, ApJ, 762, 109
Benítez N., 2000, ApJ, 536, 571
Bernstein G. M., Jarvis M., 2002, AJ, 123, 583
Bhattacharya S., Habib S., Heitmann K., Vikhlinin A., 2013, ApJ, 766, 32
Blazek J., Mandelbaum R., Seljak U., Nakajima R., 2012, J. Cosmology Astropart. Phys., 5, 041
Bleem L. E., et al., 2015, ApJS, 216, 27
Bocquet S., Saro A., Dolag K., Mohr J. J., 2016, MNRAS, 456, 2361
Brainerd T. G., Blandford R. D., Smail I., 1996, ApJ, 466, 623
Broadhurst T. J., Taylor A. N., Peacock J. A., 1995, ApJ, 438, 49
Cavagnolo K. W., Donahue M., Voit G. M., Sun M., 2009, ApJS, 182, 12
Clampitt J., Jain B., 2015, MNRAS, 454, 3357
Corless V. L., King L. J., 2009, MNRAS, 396, 315
Coupon J., Broadhurst T., Umetsu K., 2013, ApJ, 772, 65
Cui W., et al., 2016a, MNRAS, 456, 2566
Cui W., et al., 2016b, MNRAS, 458, 4052
Dawson K. S., et al., 2013, AJ, 145, 10
Diemer B., Kravtsov A. V., 2014, ApJ, 789, 1

Diemer B., Kravtsov A. V., 2015, ApJ, 799, 108

Dietrich J. P., et al., 2014, MNRAS, 443, 1713

Du W., Fan Z., Shan H., Zhao G.-B., Covone G., Fu L., Kneib J.-P., 2015, ApJ, 814, 120

Dutton A. A., Macciò A. V., 2014, MNRAS, 441, 3359

Einasto J., 1965, Trudy Astrofizicheskogo Instituta Alma-Ata, 5, 87

Eisenstein D. J., et al., 2011, AJ, 142, 72

Evrard A. E., Arnault P., Huterer D., Farahi A., 2014, MNRAS, 441, 3562

Farahi A., Evrard A. E., Rozo E., Rykoff E. S., Wechsler R. H., 2016, MNRAS, 460, 3900

Feldmann R., et al., 2006, MNRAS, 372, 565

Fischer P., et al., 2000, AJ, 120, 1198

Ford J., Hildebrandt H., Van Waerbeke L., Erben T., Laigle C., Milkeraitis M., Morrison C. B., 2014, MNRAS, 439, 3755

Foreman-Mackey D., Hogg D. W., Lang D., Goodman J., 2013, PASP, 125, 306

Han J., et al., 2015, MNRAS, 446, 1356

Hirata C., Seljak U., 2003, MNRAS, 343, 459

Hoekstra H., Jain B., 2008, Annual Review of Nuclear and Particle Science, 58, 99

Hoekstra H., Herbonnet R., Muzzin A., Babul A., Mahdavi A., Viola M., Cacciato M., 2015, MNRAS, 449, 685

Hu W., 2002, Phys. Rev. D, 66, 083515

Hu W., Kravtsov A. V., 2003, ApJ, 584, 702

Huterer D., 2002, Phys. Rev. D, 65, 063001

Johnston D. E., et al., 2007a, preprint, (arXiv:0709.1159)

Johnston D. E., Sheldon E. S., Tasitsiomi A., Frieman J. A., Wechsler R. H., McKay T. A., 2007b, ApJ, 656, 27

Kilbinger M., et al., 2013, MNRAS, 430, 2200

Leauthaud A., et al., 2010, ApJ, 709, 97

Li R., et al., 2016, MNRAS, 458, 2573

Mandelbaum R., et al., 2005, MNRAS, 361, 1287

Mandelbaum R., Seljak U., Hirata C. M., 2008a, J. Cosmology Astropart. Phys., 8, 006

Mandelbaum R., et al., 2008b, MNRAS, 386, 781

Mandelbaum R., Seljak U., Baldauf T., Smith R. E., 2010, MNRAS, 405, 2078

Mandelbaum R., Hirata C. M., Leauthaud A., Massey R. J., Rhodes J., 2012, MNRAS, 420, 1518

Mandelbaum R., Slosar A., Baldauf T., Seljak U., Hirata C. M., Nakajima R., Reyes R., Smith R. E., 2013, MNRAS, 432, 1544

Massey R., Kitching T., Richard J., 2010, Reports on Progress in Physics, 73, 086901

McKay T. A., et al., 2001, ArXiv Astrophysics e-prints,

Mehrtens N., et al., 2012, MNRAS, 423, 1024

Melchior P., Sutter P. M., Sheldon E. S., Krause E., Wandelt B. D., 2014, MNRAS, 440, 2922

Miyatake H., More S., Takada M., Spergel D. N., Mandelbaum R., Rykoff E. S., Rozo E., 2016, Physical Review Letters, 116, 041301

Nakajima R., Mandelbaum R., Seljak U., Cohn J. D., Reyes R., Cool R., 2012, MNRAS, 420, 3240

Navarro J. F., Frenk C. S., White S. D. M., 1996, ApJ, 462, 563

Navarro J. F., Frenk C. S., White S. D. M., 1997, ApJ, 490, 493

Noh Y., Cohn J. D., 2012, MNRAS, 426, 1829

Okabe N., Smith G. P., 2015, preprint, (arXiv:1507.04493)

Piccinotti G., Mushotzky R. F., Boldt E. A., Holt S. S., Marshall F. E., Serlemitsos P. J., Shafer R. A., 1982, ApJ, 253, 485

Planck Collaboration et al., 2014, A&A, 571, A29

Refregier A., 2003, ARA&A, 41, 645

Reyes R., Mandelbaum R., Gunn J. E., Nakajima R., Seljak U., Hirata C. M., 2012, MNRAS, 425, 2610

Rowe B. T. P., et al., 2015, Astronomy and Computing, 10, 121

Rozo E., Rykoff E. S., 2014, ApJ, 783, 80

Rozo E., et al., 2009a, ApJ, 699, 768

Rozo E., et al., 2009b, ApJ, 703, 601

Rozo E., Wu H.-Y., Schmidt F., 2011, ApJ, 735, 118

Rozo E., et al., 2015a, MNRAS, 450, 592

Rozo E., Rykoff E. S., Becker M., Reddick R. M., Wechsler R. H., 2015b, MNRAS, 453, 38

Rykoff E. S., et al., 2012, ApJ, 746, 178

Rykoff E. S., et al., 2014, ApJ, 785, 104

Rykoff E. S., Rozo E., Keisler R., 2015, preprint, (arXiv:1509.00870)

Rykoff E. S., et al., 2016, ApJS, 224, 1

Saro A., et al., 2015, MNRAS, 454, 2305

Schaller M., et al., 2015, MNRAS, 451, 1247

Schmidt F., Rozo E., Dodelson S., Hui L., Sheldon E., 2009, Physical Review Letters, 103, 051301

Schneider P., 2006, in Meylan G., Jetzer P., North P., Schneider P., Kochanek C. S., Wambsganss J., eds, Saas-Fee Advanced Course 33: Gravitational Lensing: Strong, Weak and Micro. pp 1–89

Sereno M., Fedeli C., Moscardini L., 2016, J. Cosmology Astropart. Phys., 1, 042

Sheldon E. S., et al., 2004a, AJ, 127, 2544

Sheldon E. S., et al., 2004b, AJ, 127, 2544

Sheldon E. S., Cunha C. E., Mandelbaum R., Brinkmann J., Weaver B. A., 2012, ApJS, 201, 32

Sifón C., Hoekstra H., Cacciato M., Viola M., Köhlinger F., van der Burg R. F. J., Sand D. J., Graham M. L., 2015, A&A, 575, A48

Simet M., Mandelbaum R., 2015, MNRAS, 449, 1259

Singh S., Mandelbaum R., More S., 2015, MNRAS, 450, 2195

Springel V., 2005, MNRAS, 364, 1105

Wechsler R. H., Zentner A. R., Bullock J. S., Kravtsov A. V., Allgood B., 2006, ApJ, 652, 71

Wright C. O., Brainerd T. G., 2000, ApJ, 534, 34

Yang X., Mo H. J., van den Bosch F. C., Jing Y. P., Weinmann S. M., Meneghetti M., 2006, MNRAS, 373, 1159

York D. G., et al., 2000, AJ, 120, 1579

van Uitert E., Gilbank D. G., Hoekstra H., Semboloni E., Gladders M. D., Yee H. K. C., 2016, A&A, 586, A43

von der Linden A., Best P. N., Kauffmann G., White S. D. M., 2007, MNRAS, 379, 867

von der Linden A., et al., 2014, MNRAS, 439, 2

APPENDIX A: DETAILS OF $\Delta\Sigma$ MODEL COMPONENTS

Our final model includes marginalization over multiple modeling issues that are secondary to the relationship we are primarily interested in measuring. We show here a simple model including none of them, and then add more complications one at a time, to better show the effect each additional parameter has on our final results. Table A1 shows the results for our MCMC model fitting for different combinations of parameters. We discuss here the various complications of the model.

Our simple model assumes no miscentring and a mass–concentration $(M - c)$ relation from the literature, Bhattacharya et al. (2013), evaluated using the publicly-available colossus package described in Diemer & Kravtsov (2015), without $M - c$ scatter. The values we obtain for the parameters, shown in Table A1, already have many of the characteristics we see in the final analysis: $\log M_0$ is somewhat above 14 and α well above 1. Our parameter values do not change significantly when we add the various complications: lognormal scatter in the mass–concentration relation with width 0.14 dex as described in the main text; a variable mass–concentration relation; miscentring; and all three. There is

Model name	No. of steps (burn-in)	Minimum $-2\ln\mathcal{L}$	d.o.f.	$\log_{10} M_0^*$	α
Simple	1000 (100)	78.41	75	$14.322^{+0.028}_{-0.029}$	$1.36^{+0.10}_{-0.09}$
Simple with $M-c$ scatter	1000 (100)	78.09	75	$14.323^{+0.028}_{-0.029}$	$1.36^{+0.09}_{-0.10}$
Fitted $M-c$ amplitude & $M-c$ scatter	1500 (100)	77.64	74	14.329 ± 0.030	$1.38^{+0.09}_{-0.10}$
Miscentring & $M-c$ scatter	1500 (100)	78.08	73	14.347 ± 0.030	$1.36^{+0.09}_{-0.10}$
Miscentring, fitted $M-c$ amplitude & $M-c$ scatter	2250 (100)	76.37	72	14.344 ± 0.031	$1.33^{+0.09}_{-0.10}$

Table A1. Fitting results for all of our cluster models, showing the parameters of scientific interest only. We report the settings for the MCMC chain and the maximum likelihood $-2\ln\mathcal{L}$ of any step in any chain for that MCMC run. We run the `emcee` MCMC ensemble sampler with 100 walkers for every chain, so the total number of steps included in the plots is 100 times what is listed here (including burn-in steps). When the Gaussian priors are not important, $-2\ln\mathcal{L}$ is equal to the χ^2. We also report the median value and the 1σ error regions (the 16th-84th percentile range) for the parameters of scientific interest. All models are NFW (Eq. 8), some with miscentring (Eq. 11), some with fitted $M-c$ relations. The last model in the table is our fiducial model used in the analysis in the main text of this work. The * symbol indicates that the mass values from the output of the MCMC chain have been corrected for model bias, as described in Section 5, and the error bar is combined statistical and systematic.

a $\sim 0.3\sigma$ decrease in α when we include all effects versus all other models, indicating that a small amount of the apparent scaling of mass with λ in the simple model can be attributed to those effects changing with the cluster richness, but the effect is small. The nuisance parameters (b and miscentring) are largely determined by our priors; c_0, the amplitude of the mass–concentration relation, shows more movement, with a value of $0.90^{+0.12}_{-0.10}$ when there is no miscentring included but $1.34^{+0.35}_{-0.25}$ when it is. Adequate modeling of the miscentring is clearly important for weak lensing studies such as these which attempt to measure the $M-c$ relation using information at scales less than the miscentring radius.

The fit quality does not vary strongly with the inclusion of more parameters, as judged by the best-fit likelihood. In summary, we can fit the redMaPPer cluster lensing signal reasonably well with a sum of NFW profiles that have characteristics determined by the input λ and redshift distribution of the redMaPPer catalogue. For the radius range and cluster distribution included in this work, including higher-level complications such as miscentring and variable mass–concentration relations are not important to obtaining a reliable mass amplitude, but do affect the scaling with richness to some extent.

APPENDIX B: REDSHIFT EVOLUTION

To test for possible redshift evolution of the mass–richness relation across our redshift range, instead of Eq. (12), we fit a model of the form

$$M = M_0 \left(\frac{\lambda}{\lambda_0}\right)^{\alpha} \left(\frac{1+z}{1+z_0}\right)^{\beta} \qquad \text{(B1)}$$

with $z_0 = 0.2$. We then perform an MCMC run of the simple model from Appendix A (with only M_0, α, scatter, and b), including this β parameter as one of the variables we want to fit, with a top-hat prior of $(-12, 2)$; the prior is asymmetric because early testing in the range $(-1, 1)$ did not reveal an obvious peak but a preference for values $\leqslant 1$, and we were unsure how low we would need to go to ensure it was included.

The value preferred for β, -1.5 ± 0.9, is consistent with our expected value of 0 at slightly above 1.5σ. The fit is better, with the minimum $-2\ln\mathcal{L} = 76.64$ instead of 78.41, but no other parameter moves significantly when β is included.

Since we expect $\beta \approx 0$ and cannot exclude this possibility using the data, we do not include redshift evolution of the mass–λ relation in the model used for our main results in this paper. Fixing $\beta = 0$ is a stronger assumption than letting β float with some prior on expected values; however, we know what fixing $\beta = 0$ does (finds the average value over all redshifts) while it is unclear what we would be modeling if we allowed β to float, so we make the tradeoff of being insensitive to redshift in favor of better understanding the physical importance of our other parameters.

APPENDIX C: THE PROJECTION RATE IN THE redMaPPer CLUSTER CATALOGUE

In section 5.3, we estimated the impact of projection effects on our weak lensing mass calibration. Our starting point in that section was the projection rate in the redMaPPer cluster catalogue. Here, we discuss how we arrived at the prior for this projection rate.

Our starting point is Rykoff et al. (2014), who set a lower limit on the incidence of these type of projection effects by placing synthetic galaxy clusters within the SDSS survey and then performing a cluster finding step. We found a richness-dependent rate of projection effects that increases with richness, reaching 5% for the richest clusters.

In practice, this fraction should be boosted due to correlated structures along the line of sight. The associated multiplicative factor η should take the form

$$\eta = \frac{\int \mathrm{d}^3 V \,(1+\xi)}{\int \mathrm{d}^3 V} \qquad \text{(C1)}$$

where ξ is the halo-halo correlation function, and the integrals are over the volume over which projection effects can occur. We model this volume as a cylinder of radius $R_{\min} \approx 2$ Mpc and a height $2\sigma_z$, where σ_z is the photometric redshift uncertainty of red galaxies. This corresponds to a cylinder height $R_{\max} \approx 130$ Mpc. Adopting a correlation function $\xi \propto r^{-2}$, and a typical cluster correlation length $R_{\mathrm{corr}} \approx 15$ Mpc we arrive at

$$\eta = 1 + \frac{R_{\mathrm{corr}}^2}{R_{\min} R_{\max}} \approx 1.8. \qquad \text{(C2)}$$

Adopting a $\sim 50\%$ systematic uncertainty for the clustering

correction, so that $\eta = 1.8 \pm 0.4$, we arrive at a total projection rate of $\eta \times 5\% = 9\% \pm 2\%$ for the highest richness clusters.

A second estimate can be made on the basis of RM IV, who find that $6\% \pm 2\%$ of the cluster richness is due to projected galaxies in excess of the background expectation. We assuming these galaxies are due to projections of two comparably rich systems, each contributing $\approx \lambda/2$ galaxies to a single blended cluster of richness λ. In this case, the fraction of projected galaxies $f = 0.06 \pm 0.02$ is given by

$$f = \frac{p n(\lambda)(\lambda/2)}{n(\lambda)\lambda} = p/2. \tag{C3}$$

where $n(\lambda)$ is the abundance of clusters of richness λ. We arrive then at $p = 12\% \pm 4\%$, in reasonable agreement with our original estimate. A simulation analysis by Kitadinis et al. (in preparation) find a similar projection rate for redMaPPer clusters in simulations.

On the basis of these arguments, we adopt a projection rate $p = 10\% \pm 4\%$.